Lasers in Surgery and Medicine 47:579–594 (2015)

Enzymatically Activated Near Infrared Nanoprobes Based on Amphiphilic Block Copolymers for Optical Detection of Cancer

Tuğba Özel, MS,[1] Sean White, PhD,[2] Elaine Nguyen, BS,[2,3] Austin Moy, PhD,[2,4] Nicholas Brenes, BS,[4,5] Bernard Choi, PhD,[2,6] and Tania Betancourt, PhD[1,5,7*]

[1]*Materials Science, Engineering, and Commercialization Program, Texas State University, San Marcos, Texas 78666*
[2]*Department of Biomedical Engineering, Beckman Laser Institute, University of California, Irvine, California 92697*
[3]*School of Medicine, Virginia Commonwealth University, Richmond, Virginia*
[4]*The University of Texas at Austin, Austin, Texas 78712*
[5]*InnoSense LLC, Torrance, California 90505*
[6]*Department of Surgery, University of California, Irvine, California 92697*
[7]*Department of Chemistry and Biochemistry, Texas State University San Marcos, Texas 78666*

Background and Objective: Nanotechnology offers the possibility of creating multi-functional structures that can provide solutions for biomedical problems. The nanoprobes herein described are an example of such structures, where nano-scaled particles have been designed to provide high specificity and contrast potential for optical detection of cancer. Specifically, enzymatically activated fluorescent nanoprobes (EANPs) were synthesized as cancer-specific contrast agents for optical imaging.

Study Design/Materials and Methods: EANPs were prepared by nanoprecipitation of blends of poly(lactic acid)-*b*-poly(ethylene glycol) and poly(lactic-co-glycolic acid)-*b*-poly(L-lysine). The lysine moieties were then covalently decorated with the near infrared (NIR) fluorescent molecule AlexaFluor-750 (AF750). Close proximity of the fluorescent molecules to each other resulted in fluorescence quenching, which was reversed by enzymatically mediated cleavage of poly(L-lysine) chains. EANPs were characterized by dynamic light scattering and electron microscopy. Enzymatic development of fluorescence was studied *in vitro* by fluorescence spectroscopy. Biocompatibility and contrast potential of EANPs were studied in cancerous and noncancerous cells. The potential of the nanoprobes as contrast agents for NIR fluorescence imaging was studied in tissue phantoms.

Results: Spherical EANPs of ~100 nm were synthesized via nanoprecipitation of polymer blends. Fluorescence activation of EANPs by treatment with a model protease was demonstrated with up to 15-fold optical signal enhancement within 120 minutes. Studies with MDA-MB-231 breast cancer cells demonstrated the cytocompatibility of EANPs, as well as enhanced fluorescence associated with enzymatic activation. Imaging studies in tissue phantoms confirmed the ability of a simple imaging system based on a laser source and CCD camera to image dilute suspensions of the nanoprobe at depths of up to 4 mm, as well as up to a 13-fold signal-to-background ratio for enzymatically activated EANPs compared to un-activated EANPs at the same concentration.

Conclusion: Nanoprecipitation of copolymer blends containing poly(L-lysine) was utilized as a method for preparation of highly functional nanoprobes with high potential as contrast agents for fluorescence based imaging of cancer. Lasers Surg. Med. 47:579–594, 2015.

Key words: biodegradable polymers; enzymatically-responsive polymers; nanomedicine; nanoparticles; near infrared fluorescent contrast agents; near infrared optical imaging; optical contrast agents; PLA-PEG; PLGA; protease activated probes

INTRODUCTION

Cancer remains one of the most prevalent diseases to date. The average 5-year survival rate for cancer patients is 68% [1], suggesting that despite great advances in diagnostics and therapeutics, there is still a great need for improved options. Patient survival rates are highly influenced by the stage at which the cancer is diagnosed [1]. Consequently, development of improved methods for detection of cancer at an early stage is of great importance.

Conflict of Interest Disclosures: All authors have completed and submitted the ICMJE Form for Disclosure of Potential Conflicts of Interest and none were reported.

Contract grant sponsor: NIH; Contract grant numbers: 1R43 CA144129-01, P41 EB015890, R01 HD065536; Contract grant sponsor: Texas Emerging Technology Fund; Contract grant sponsor: Welch Foundation; Contract grant number: AI-0045; Contract grant sponsor: Arnold and Mabel Beckman Foundation.

*Correspondence to: Tania Betancourt, PhD, Department of Chemistry and Biochemistry, and Materials Science, Engineering and Commercialization Program. Texas State University, 601 University Drive, San Marcos, TX 78666.
E-mail: TB26@txstate.edu

Accepted 1 July 2015
Published online 17 July 2015 in Wiley Online Library (wileyonlinelibrary.com).
DOI 10.1002/lsm.22396

NIR optical imaging has emerged recently as a viable alternative for the detection, monitoring, and image-guided resection of tumors [2–4]. Imaging in the NIR region (700–1,000 nm) is advantageous since absorption of most biological chromophores, including oxyhemoglobin, deoxyhemoglobin, melanin, and fat in this region is minimal [5,6]. Imaging-based detection of tumors at early stages via fluorescence methods is limited by the low fluorescence contrast between normal and cancerous tissue. Use of probes targeted to or activated by the disease is a promising approach for creating sufficient contrast [6].

Significant work has been done in the development of fluorescent probes that can provide disease specificity and increased signal-to-noise ratio through an activation mechanism. Among these, macromolecular protease-triggered NIR fluorescent probes have been used as effective triggered fluorescent contrast agents for cancer. Weissleder and co-workers developed NIR conjugate probes for *in vivo* imaging of tumors with high protease activity by the conjugation of the fluorescent dye Cy5.5 to poly(L-lysine) chains [7,8]. This work demonstrated the ability of tumor lysosomal proteases to cleave the conjugate to develop NIR signal *in vivo*. The effectiveness of these systems has been demonstrated in preclinical models of metastatic ovarian cancer [9], esophageal cancer [10], gastric cancer [11], and sarcoma [12,13]. These systems have also been utilized for detection and imaging of other diseases associated with changes in enzymatic activity of the tissue, including inflammation and vascular disease [14–22].

Few investigations have been performed in the formulation of activatable NIR fluorescent probes in nanoparticle format [23–28]. The use of nanoparticles can improve tumor targeting via passive and active targeting, taking advantage of the enhanced permeability and retention (EPR) effect, and by permitting concurrent incorporation of targeting moieties with high affinity to tumor cell biomarkers. The EPR effect is due to a combination of leaky angiogenic blood vessels with 100 nm–2 μm pores that allow the extravasation of nano-sized particles [29], and deficient tumor lymphatics that allow particle accumulation at cancerous tissue [29–32]. In addition, because of their macromolecular design, nanoparticles allow incorporation of a range of functionalities into a discrete entity. The benefits of nanoparticles in bioimaging and therapeutic applications have been previously explored with gold nanoparticles, nanoshells, nanorods, and nanohorns as photothermal agents [33–38].

In the present work, we developed methods for facile preparation of a contrast agent for fluorescence-based imaging of tumors that could: (i) take advantage of the benefits of nanomedicine, including the ability to carry a high payload of the imaging agent to target tumors, and (ii) provide a mechanism for tumor-mediated activation of fluorescence. Specifically, enzymatically activated nanoprobes (EANPs) that easily assemble from well-characterized biocompatible polymers were developed and evaluated *in vitro* as contrast agents for highly specific fluorescence imaging in cancer. These nanoprobes utilize protease-labile polypeptides labeled with NIR fluorophores as a mean to provide an off-on switch for fluorescence development that is triggered by tumor-overexpressed enzymes.

MATERIALS AND METHODS

EANPs, consisting of a core-shell structure (Fig. 1), were prepared by nanoprecipitation of amphiphilic block copolymers. The hydrophobic core, which could be used for delivery of chemotherapeutic or additional imaging agents, is made of the biodegradable and biocompatible

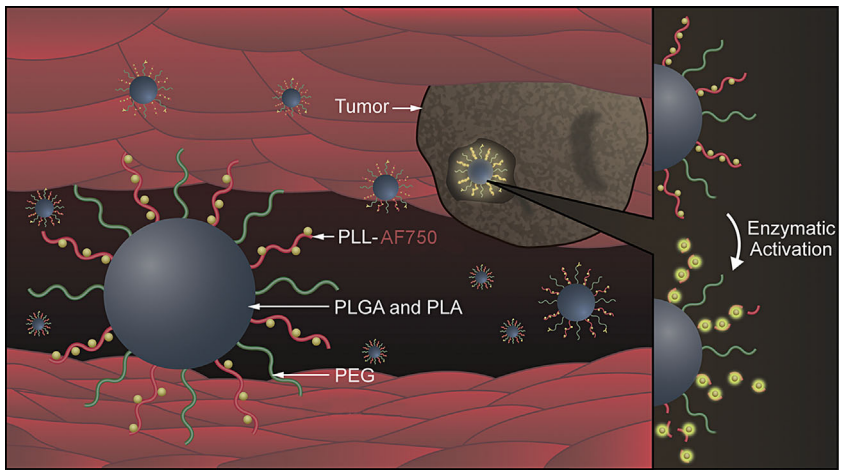

Fig. 1. Design and function of enzymatically activated nanoprobes (EANPs). EANPs are prepared by nanoprecipitation of blends of amphiphilic PLA-PEG and PLGA-PLL copolymers. Near infrared fluorescent molecules covalently attached to PLL chains are initially quenched. Protease-mediated cleavage of PLL chains induces fluorescence activation by allowing their dispersion in the physiological medium.

polymers poly(lactic-co-glycolic acid) (PLGA) and poly-(lactic acid) (PLA). The surface of EANPs contains the hydrophilic polymers poly(ethylene glycol) (PEG) and poly-L-lysine (PLL). PEG increases residence time of probes in the circulation [39] by acting as a shield against adsorption of opsonin biomolecules and the consequent rapid recognition and removal by the reticuloendothelial system (Kuppfer cells and macrophages) [40]. Because of the high flexibility and water-binding ability of PEG, it is able to sterically stabilize nanoparticle suspensions and hinder their interaction with plasma proteins and the immune system [41–44]. Finally, PLL acts as a protease cleavable anchor for NIR fluorophores, as previously utilized in peptide-based NIR probes [7–9]. PLL is a model polypeptide that can be cleaved by proteolytic enzymes commonly overexpressed by tumors, such as cathepsin B and D. Close-packed binding of NIR fluorophores to the PLL backbone results in fluorescence quenching due to processes such as non-radiative energy transfer. Enzymatic cleavage of PLL results in increased mobility and space between fluorophores, resulting in fluorescence activation (Fig. 1, inset).

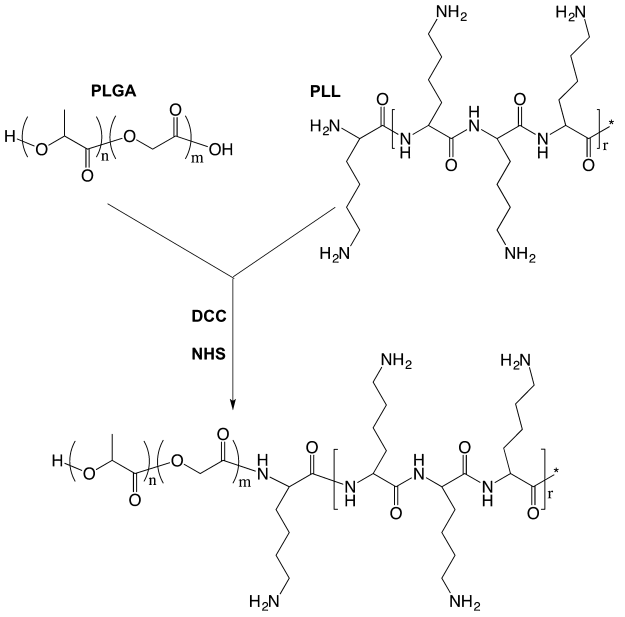

Fig. 2. Synthesis of PLGA-PLL. This copolymer was synthesized by carbodiimide-mediated coupling of acid-terminated PLGA and PLL.

Materials

PLGA with terminal carboxylic acid groups (5050 DLG 2A, MW 16,000 Da) was acquired from Lakeshore Biomaterials (Birmingham, AL). Bifunctional poly(ethylene glycol) with hydroxyl and carboxylic acid terminal groups (OH-PEG-COOH, Mn 3,400 Da) was obtained from Laysan Bio (Arab, AL). Poly(ethylene glycol) methyl ether (OH-PEG-OMe, Mn 5,000 Da), 3,6-dimethyl-1,3-dioxane-2,5-dione (lactide), Trypsin solution from porcine pancreas, *N*,*N*′-dicyclohexylcarbodiimide (DCC), *N*-hydroxysuccinimide (NHS), poly-L-lysine hydrobromide (PLL, MW 1,000–5,000 Da), N_{α}-tosyl-L-lysine chloromethyl ketone (TLCK), and *N*-(dimethylaminopropyl)-*N*′-ethylcarbodiimide HCl (EDC) were purchased from Sigma–Aldrich (St. Louis, MO). Alexa Fluor 750 carboxylic acid succinimidyl ester (AF750) was obtained from Molecular Probes (Invitrogen, Carslbad, CA). All organic solvents used were of at least reagent grade. Deionized water (DI H_2O) was produced with a Millipore Direct Q system.

Synthesis of PLGA-PLL Copolymer

PLGA-PLL copolymers were prepared by activation of carboxylated PLGA into primary amine-reactive *N*-hydroxysuccinimide esters via carbodiimide chemistry (Fig. 2). Activated PLGA formed amide bonds upon conjugation with PLL primary amine groups. PLGA (1 g) was dissolved in 10 ml of chloroform. To this solution, 129 mg of DCC and 72 mg of NHS (PLGA:DCC:NHS molar ratio of 1:10:10) were added and allowed to react overnight at room temperature. Urea byproduct was filtered using a 0.2 μm syringe filter. The activated PLGA was recovered from the solution by precipitation in diethyl ether, centrifuged and rapidly dried under vacuum. Activated PLGA (0.8 g) was then immediately dissolved in dimethylsulfoxide or dimethylformamide and reacted with 125 mg of PLL (PLGA/PLL molar ratio of 2:1 using an average PLL molecular weight of 4,000 Da) in the presence of triethylamine (TEA) (PLL:TEA molar ratio of 1:40). After 24 hours, the copolymer was precipitated in DI H_2O and centrifuged. The polymer pellet was dissolved in acetone, precipitated in DI H_2O and centrifuged two more times to remove unbound, water-soluble PLL and remaining byproducts. The polymer was then dried under vacuum and stored desiccated at −20°C. Fourier transform infrared spectroscopy (FTIR) and ^{1}H nuclear magnetic resonance (^{1}H-NMR) were used for characterization of the copolymer. For FTIR analysis, a Nicholet 380 FTIR spectrometer with attenuated total reflectance (ATR) attachment and a Bruker Tensor 27 FTIR with ATR were used. For NMR characterization, a Bruker AMX-500 NMR (Numega Resonance Laboratories, San Diego, CA) and a Bruker Avance 400 MHz FT NMR were used.

Preparation of PLA-PEG-COOH and PLA-PEG-OMe

Two types of PEG were used in the preparation of EANPs: Methoxy (—O—CH_3)-terminated PEG (PEG-OMe) acts as a stabilizing polymer. PEG terminated in carboxylic acid groups (PEG-COOH) was used to provide a site for covalently binding targeting antibodies to EANPs in future work. PLA-PEG-COOH and PLA-PEG-OMe were prepared by the ring opening polymerization of lactide initiated by terminal hydroxyl groups of heterofunctional PEGs (Fig. 3) [45]. Prior to polymerization, lactide was recrystallized from hot ethyl acetate. Recrystallized lactide and PEG (either PLA-PEG-COOH or PLA-PEG-OMe) were placed in an oven-dried, two-necked reaction flask. Toluene was added and the flask was heated to 110°C with

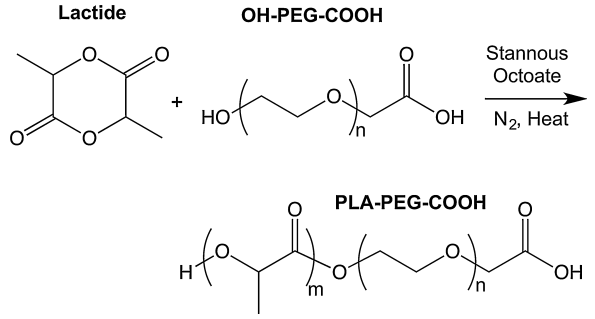

Fig. 3. Synthesis of PLA-PEG block copolymers. PLA-PEGs were prepared by the ring opening polymerization of lactide on terminal PEG hydroxyl groups. Here the reaction is shown for the formation of PLA-PEG-COOH. Polymerization of PLA-PEG-OMe occurs similarly.

a silicon oil bath. Nitrogen or argon was bubbled into the solution throughout the process. The polymerization was allowed to occur for 2–4 hours, during which an increase in the content's viscosity was observed. The reaction was then stopped by rapid cooling and the polymer was recovered by precipitation in diethyl ether. For further purification, the polymer was re-dissolved in acetone and precipitated in diethyl ether two additional times. The polymer was then dried under vacuum and stored desiccated at -20°C. FTIR and NMR were used for characterization of the copolymer.

Preparation of EANPs

EANPs were prepared via nanoprecipitation [45,46] of copolymer blends. PLGA-PLL, PLA-PEG-COOH, and PLA-PEG-OMe were dissolved in acetone separately at 50 mg/ml. These solutions were combined in the following volume ratios: 500 μl PLGA-PLL, 125 μl PLA-PEG-COOH, and 125 μl PLA-PEG-OMe. An additional 2 ml of acetone were added. The copolymer solution was then added dropwise to 5 ml of a stirring aqueous solution of 10 mg/ml bovine serum albumin. EANPs formed spontaneously as a result of the migration of the water miscible solvents into the aqueous phase, and the consequent precipitation of the hydrophobic regions of the copolymers (PLGA and PLA). The solvent was evaporated under mild vacuum. EANPs were washed three times with DI H_2O by centrifugation at $34{,}500\times g$ for 20 minutes using sonication to resuspend the pellets. EANP suspensions (4.4 mg/ml) were stored at 4°C.

The size of EANPs was determined by dynamic light scattering (DLS) using a Malvern Zetasizer upon dilution in phosphate buffered saline (PBS, pH 7.4). Transmission electron microscopy (TEM) and scanning electron microscopy (SEM) were used to confirm the size and morphology of EANPs. The composition of dry EANP powder was probed via FTIR.

Conjugation of Fluorescent Dye to EANPs

AF750 was conjugated to surface PLL chains on EANPs. For this process, 4 ml of EANPs were reacted with 0.4 mg of AF750 for 12 hours in the dark at room temperature. The NHS ester of AF750 reacts with primary amines on PLL forming stable amide bonds. The close proximity and high concentration of PLL-bound AF750 on the surface of EANPs resulted in fluorescence quenching. EANPs were purified by centrifugation and washed with DI H_2O three times to remove unbound AF750. The highly-colored AF750-labeled EANPs were characterized by absorption and fluorescence spectroscopy, and their size by DLS.

For some of the cell microscopy studies, EANPs were labeled with fluorescein isothiocyanate (FITC-EANPs) instead of AF750 to allow use of typical microscope light source, optical filters, and camera. Specifically, EANPs were suspended in 0.1 M sodium carbonate buffer (pH 9.0) and reacted with FITC at room temperature. The labeled FITC-EANPs were washed with DI H_2O by centrifugation until the supernatant was clear.

Enzymatic Activation of EANP Fluorescence

A Photon Technology International, Inc., QM4 spectrofluorometer was used for fluorescence characterization. AF750-labeled EANP suspensions were diluted in DI H_2O to 1/10th the stock concentration and a volume of 250 μl of this suspension was placed in a quartz microcuvette (CH Instruments, Inc.). Additional 200 μl of PBS buffer (pH 7.4) was added. To this solution, 50 μl of 25.0 or 0.25 mg/ml trypsin in PBS was added (final trypsin concentration in sample of 2.5 or 0.025 mg/ml). Fluorescence readings were taken with the starting sample, after PBS addition, after trypsin addition (time zero), and at specific times after this to study the rate and extent of fluorescence development. Fluorescence spectra were obtained in the range of 750–900 nm ($\lambda_{EX} = 740$ nm). Samples were protected from light at all time points except during fluorescence measurements. Control solutions (ruthenium bathophenanthroline in dimethylformamide) were simultaneously analyzed to verify constant fluorescence output for non-enzymatically activated samples. Similar studies were carried out with FITC-EANPs.

Similar studies were performed with a Biotek H4 multimode plate reader ($\lambda_{EX} = 740$ nm, $\lambda_{EM} = 775$ nm) to demonstrate the reproducibility of fluorescence enhancement. Studies were conducted in 96-well plates. Four repetitions were done for each sample. Controls consisted of EANPs that were incubated with PBS buffer only, or EANPs exposed to trypsin together with the protease inhibitor TLCK. Fluorescence readings were normalized with respect to the control consisting of EANPs exposed to PBS only. Data are presented as the average of four replicates that were analyzed per sample. Student's t-tests were performed to establish statistically significant differences between samples based on a confidence level of 95% ($P < 0.05$).

Cell Culture

MDA-MB-231 human mammary adenocarcinoma cells were obtained from the American Type Tissue Collection (ATCC). MDA-MB-231 cells are known to produce high

levels of cathepsins [47]. Adult human dermal fibroblasts (HDF) were generously donated by Dr. Brian Wong, University of California, Irvine. HDF cells were originally harvested from normal human facial skin as previously described [48]. Cell harvesting was conducted in adherence to the guidelines of the Institutional Review Board at the University of California, Irvine. HDF cells were chosen as a non-cancerous control cell line. Cells were cultured in Dulbecco's Modified Eagle's Medium (DMEM) with 10% bovine serum in an incubator at 37°C and under a CO_2 atmosphere.

Determination of EANP Cytocompatibility

MDA-MB-231 cells were plated at 5,000 cells/well in 96-well plates with 100 μl of complete cell culture media. Peripheral wells were filled with sterile, buffered saline solution to maintain appropriate humidity. After 24 hours of incubation, the growth medium was replaced with suspensions of AF750-labeled EANPs in complete medium in the concentration range of 1 to 1,000 μg/ml. The cells were then incubated at 37°C and 5% CO_2 for 72 hours. Wells with cells not exposed to EANPs functioned as the positive cytocompatibility controls, while wells with cells treated with 100 μl of methanol for 15 minutes served as the negative cytocompatibility controls.

The viability of the cells was determined using the MTT assay. The media was replaced with 100 μl 0.5 mg/ml MTT reagent (Thiazolyl Blue Tetrazolium Bromide, Sigma–Aldrich) in growth medium. The cells were incubated for an additional 3.5 hours. The media was then carefully removed and the resulting formazan crystals were dissolved in 100 μl of dimethyl sulfoxide. The peak absorbance of formazan was read at 590 nm with a Biotek H4 multi-mode plate reader. The average absorbance values were corrected by subtracting the average baseline absorbance at 700 nm. Averages and standard deviations were calculated from the measurements of six wells for each condition. Viability was calculated as a percentage of the positive cytocompatibility control. Student's *t*-tests were performed to establish statistically significant differences between samples based on a confidence level of 95% ($P < 0.05$).

Microscopic Study of EANP Interaction With Cells

For initial studies, MDA-MB-231 and HDF cells were plated at a density of 60,000 cell/ml per well on 8-well Lab-Tek™ chambered coverglass. After 24 hours, cells were incubated with Advanced DMEM growth medium for 1–2 hours to equilibrate them for the studies. Two wells were used per condition. Wells containing only cells served as the negative controls. Cells were exposed to FITC-labeled EANPs at 1 mg/ml. Wells were randomly filled one at a time. A Zeiss LSM 510 confocal microscope with a 488 nm laser was used for imaging the cells. Reflectance and fluorescence images were obtained following nanoprobe addition and after multiple washes to remove unbound or uninternalized FITC-labeled EANPs.

Separate studies were conducted with only MDA-MB-231 cells to assess the degree to which observed fluorescence was associated with enzymatic development, and that near infrared fluorescence could in fact be observed. For these studies, MDA-MB-231 cells were plated on 8-well Lab-Tek chambered coverslips at a density of 50,000 cells per well in 0.3 ml of media. The cells were grown under normal culture conditions 24 hours prior to microscopy studies. To begin the study, the media was replaced with AF750-labeled EANPs at a concentration of 500 μg/ml in the presence of varying concentrations (7.8–250 μM) of the protease inhibitor TLCK. Cells exposed to EANPs in the absence of the inhibitor were used as positive controls, while cells incubated with media only (no EANPs and no TLCK) were used as negative controls. The cells were incubated under normal growth conditions for 48 hours, after which they were washed three times with Dulbeccos' phosphate buffered saline and immediately imaged with a AMG EVOS® FL LED-based microscope utilizing a Cy-7 filter cube (Ex: 710/40, Em: 775/46, optimal for AF750 per manufacturer).

In Vitro NIR Imaging in Phantoms

Imaging of AF750-EANP suspensions within tissue phantoms was performed to determine if fluorescence from dilute concentrations of EANPs was detectable with a NIR imaging instrument and the depth-dependence of the minimum-resolvable concentration. The imaging system consisted of a Photometrics QuantEM electron-multiplying charged coupled device (EMCCD) camera with Nikon Micro-Nikkor 105 mm lens (f/2.8). For the excitation source, a 1 W Biolitec laser ($\lambda = 664$ nm) light source was used. A ground-glass diffuser was used to diffuse the excitation light. An 800-nm long pass filter (Thorlabs FEL800) was placed between the lens and the camera to isolate the fluorescence emission from EANPs. A silicone phantom designed with optical properties similar to those of dermis at NIR wavelengths was used [49]. The phantom contained refillable tubes of ~0.35 mm inner diameter located at center depths of 1, 2, 3, and 4 mm from the surface. In the studies, AF750-labeled EANP suspensions (1 mg/ml) were incubated with trypsin (final concentration of 2.5 mg/ml) for 2 hours prior to dilution with PBS and subsequent imaging to achieve fluorescence enhancement. Negative control samples of EANPs were not exposed to trypsin but simply diluted in PBS to the appropriate concentration. Approximately 0.1 ml of the activated EANP suspension was injected into each of the tubes. Multiple EANP concentration ranges were imaged within the same tissue phantom.

Fluorescence data was collected using Micro-Manager 1.4 software at an exposure time of 2 seconds. Data represent the average number of detector counts within an 8×200 pixel region of interest centered along the sample length. Data were corrected for background fluorescence of saline solutions that were imaged in between samples. Error bars represent the standard deviation of the counts within each region of interest.

RESULTS

Synthesis of PLGA-PLL Copolymer

Qualitatively, conjugation was noted by the *quasi*-micellar behavior of the copolymer upon precipitation in water. The composition of PLGA-PLL copolymer was analyzed by FTIR and ^{1}H-NMR. Figure 4 shows the FTIR spectra of the PLGA-PLL and PLA-PEG copolymers prepared. Figure 4A specifically shows the FTIR spectra of PLGA, PLL, and PLGA-PLL copolymer. PLL spectra are characterized by a strong carbonyl stretch peak at 1,680–1,640 cm^{-1} (amide I band), a broad and strong NH bend (amide II band) peak at 1,560–1,630 cm^{-1}, medium amide C—N stretch peaks at 1,310–1,290 cm^{-1}, medium amide NH stretch peak at 3,300–3,280 cm^{-1}, broad medium band for NH stretch of primary amines at 3,460–3,280 cm^{-1}, and alkyl CH stretch and CH_2 deformations at 2,980–2,850 and 1,470–1,450 cm^{-1}, respectively. Due to the hygroscopic nature of PLL, the broad OH stretch peak also influences PLL's spectrum. The spectrum of PLGA shows the characteristic ester carbonyl stretch absorption peak at 1,765–1,720 cm^{-1}, C—O—C stretch peak at 1,290–1,180 cm^{-1}, and alkyl CH stretch and CH_2 deformations at 2,980–2,850 and 1,470–1,450–cm^{-1}, respectively. PLL C=O stretch and amide II NH bend peaks (indicated by arrows), and PLGA carbonyl stretch absorption peaks at 1,745 cm^{-1} are clearly seen in the PLGA-PLL copolymer spectrum, confirming the presence of both blocks in the copolymer.

NMR confirmed the presence of PLGA and PLL in the copolymer, although accurate quantification of the conjugation extent was not possible due to peak overlap. Figure 5 displays the ^{1}H-NMR spectra of PLL in D_2O, and of PLGA and PLGA-PLL in deuterated dimethylsulfoxide (DMSO-d6). PLL proton peaks are assigned as follows: β, γ, and δ protons at 1.2–2.2 ppm (6 H), ε methane protons at ~ 3 ppm (2 H), and α proton at 4.0–4.5 ppm (1 H) [50]. PLGA proton peaks correspond to lactide methane quartets and methyl doublets at δ 5.2 (1 H) and 1.6 ppm (3 H), respectively, and glycolide methane protons δ 4.8 ppm (2 H).

Preparation of PLA-PEG-COOH and PLA-PEG-OMe

FTIR was used to confirm the structure of the amphiphilic PLA-PEG-COOH and PLA-PEG-OMe copolymers, as shown in Figure 4B. The copolymers present peaks for alkyl (2,800–2,950 cm^{-1}) and ether C—O—C stretch (~1,100 cm^{-1}) associated with the PEG block. However, they also present the characteristic C=O stretch peak (~1,710–1,680 cm^{-1}) of the PLA polyester block in addition to further alkyl absorption peaks at 2,950–3,000 cm^{-1}. Proton NMR also confirmed the polymer composition and was used to estimate the molecular weight of the polymer by comparing the area under the peak of the PEG protons at 3.6 ppm that of the polymerized poly(lactide) peaks at 1.6 and 5.2 ppm as previously reported [45]. A molecular weight of 19,000 Da was calculated in this manner (NMR spectra not shown).

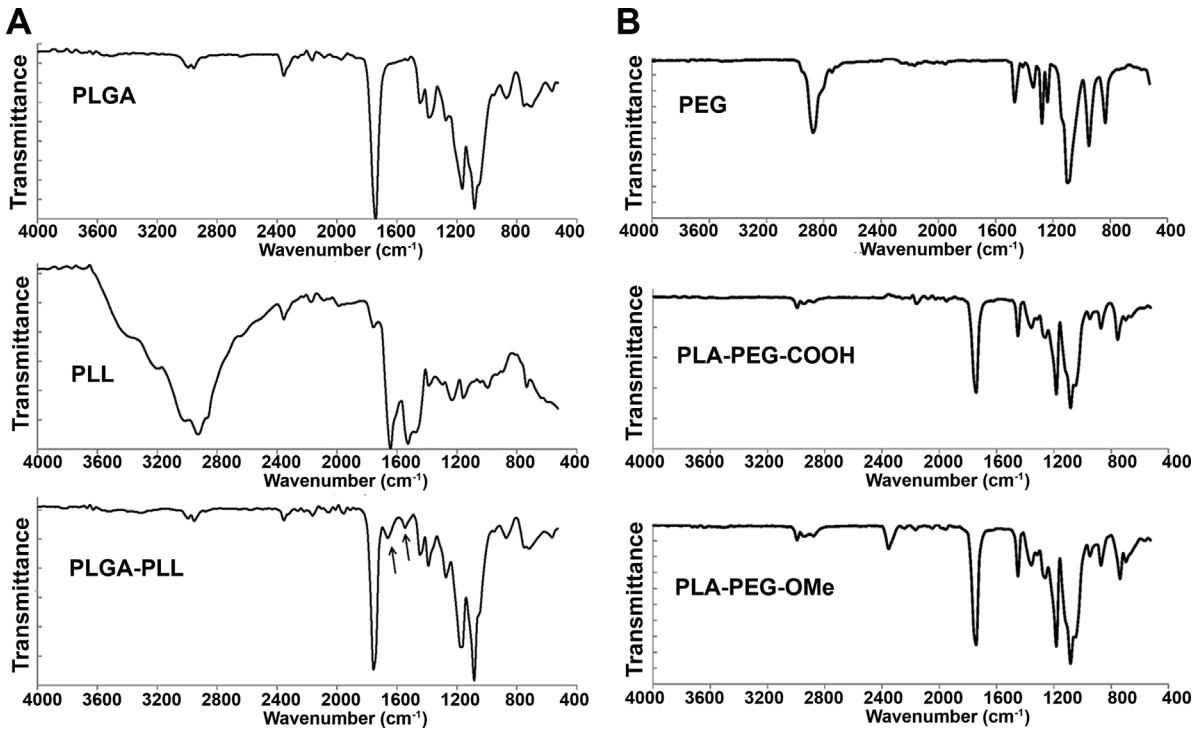

Fig. 4. FTIR spectra of synthesized copolymers. **A**: PLL, PLGA, and PLGA-PLL. Arrows in PLGA-PLL spectrum indicate the presence of PLL C=O stretch and amide NH bend peaks in the copolymer. **B**: PEG, PLA-PEG-COOH, and PLA-PEG-OMe. The FTIR spectra of the copolymers demonstrate the presence of all expected polymer blocks.

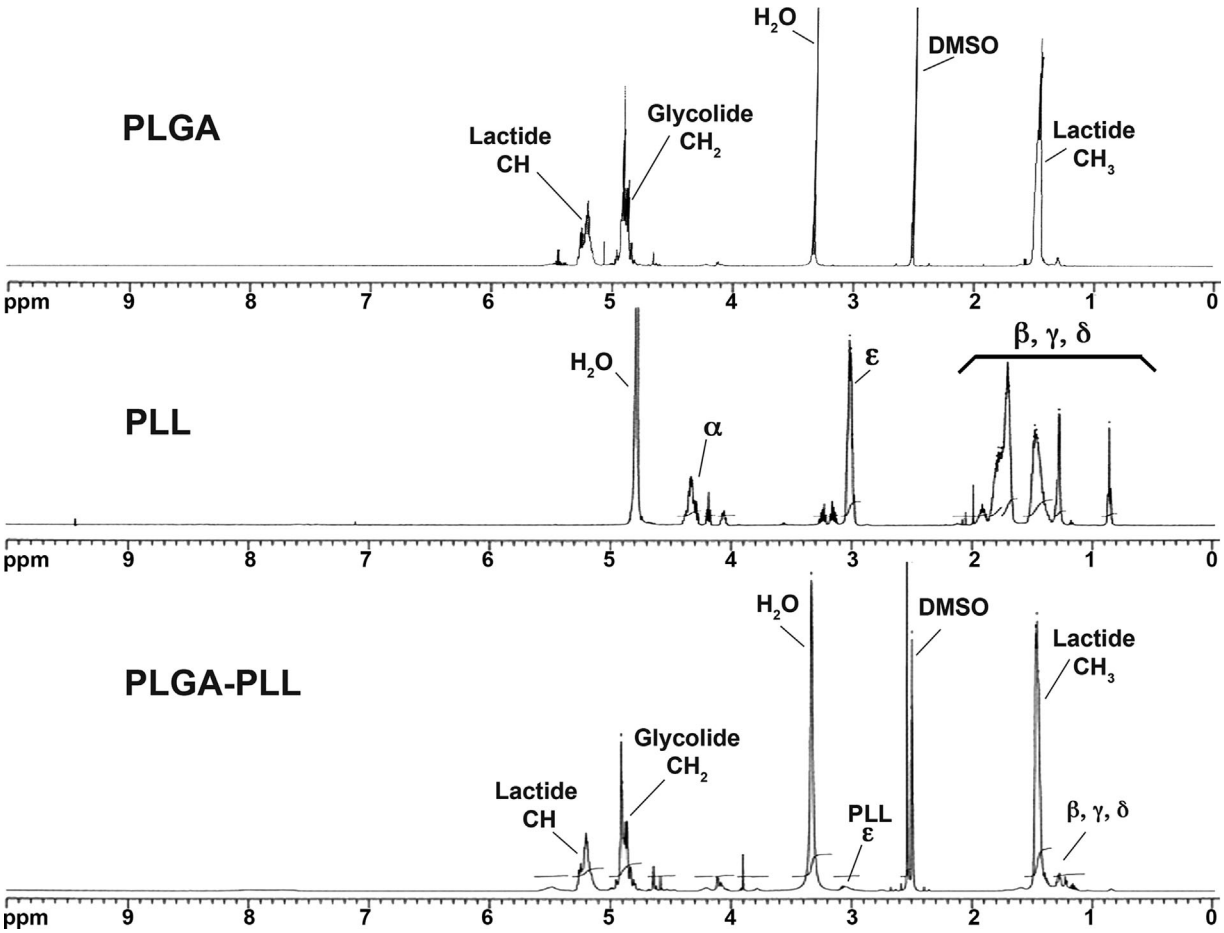

Fig. 5. ^{1}H-NMR of PLGA, PLL, and PLGA-PLL. NMR spectra of the copolymer presents the peaks associated with the original polymer blocks.

Preparation of Nanoprobes

EANPs were successfully prepared via nanoprecipitation. Figure 6 summarizes the characteristics of these nanoprobes. Figure 6A shows SEM images of the EANPs after attachment of AF750. Spherical EANPs of about 50–120 nm in diameter are observed. Figure 6B shows the dynamic light scattering (DLS) size distribution of representative batches of EANPs before and after AF750 conjugation. The hydrodynamic diameter of the particles after purification via centrifugation was in the range of 70–200 nm, with an average of about 100 nm. Sizing studies were performed by dynamic light scattering for more than nine batches before fluorophore conjugation or after conjugation of FITC or AF750. The fact that consistent sizing was obtained between batches demonstrates the reproducibility of the procedure. An overall size increase was also noticed upon fluorophore conjugation via DLS, possibly as a result of increased surface hydrophobicity leading to increased aggregation potential. Polydispersity indexes ranged from 0.05–0.11 before centrifugation to 0.11–0.17 after AF750 conjugation and purification. Figure 6C shows transmission electron microscopy images of the EANPs stained with uranyl acetate, which corroborate the size and shape of the EANPs.

The conjugation of AF750 to the PLL chains on the surface of the EANPs was confirmed visually. Figure 6D shows images of AF750-conjugated EANPs as a pellet at the last step of purification via centrifugation and as a suspension in PBS. Note the intense color of the pellet and the lack of AF750 in the supernatant on the left image, demonstrating effective covalent conjugation to the surface of the EANPs.

The composition of the EANPs was analyzed via FTIR to confirm the presence of the various copolymers used in their preparation. Absorption peaks associated with PLA/PLGA, PEG, and PLL were recognizable in the FTIR spectrum of EANPs as expected (Fig. 6E). Specifically, strong absorption peaks at 2,940 cm^{-1} and 850 cm^{-1} attributed to PEG blocks, and a strong peak at 1,760 cm^{-1} associated with PLA and PLGA polyester carbonyl groups were observed. Finally, the peak at 1,660 cm^{-1} associated with PLL amide carbonyl stretch was clearly visible.

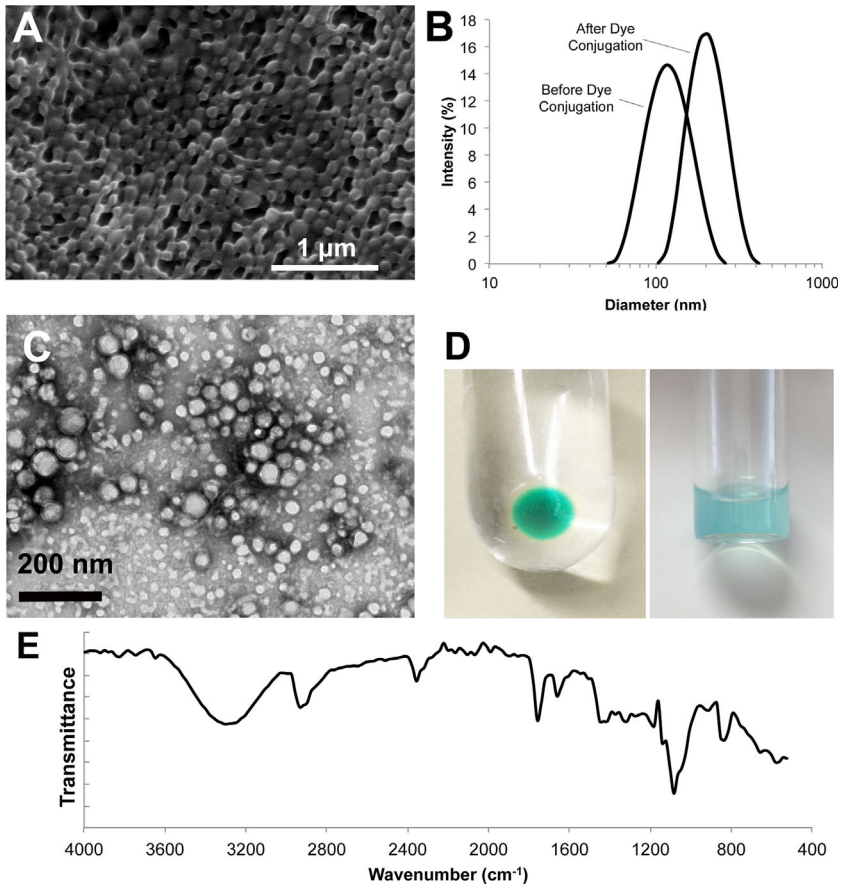

Fig. 6. EANP Characterization. **A**: Scanning electron microscopy images of EANPs after AF750 attachment. **B**: Intensity-weighted size distribution of EANPs before and after AF750 conjugation. **C**: Transmission electron microscopy image of EANPs. **D**: Image of centrifuged AF750-labeled EANPs on last wash step and of EANP suspension. **E**: FTIR spectrum of freeze dried EANPs.

Enzymatic Activation of Fluorescence

Trypsin from porcine pancreas was used as a model protease for activation of the fluorescence of the AF750-labeled EANPs *in vitro*. When exposed to 2.5 mg/ml trypsin, the peak fluorescence intensity of EANP suspensions immediately increased threefold and reached almost 15-fold within 120 min (Fig. 7A). It should be noted that the fluorescence level of the EANPs at these conditions was not measured at times greater than 2 hours; thus, it is expected that a higher level of fluorescence intensity would be possible. In contrast, the same batch of EANPs showed no increase in fluorescence in the absence of trypsin (control with equivalent volume of PBS) or only a slight increase when simultaneously incubated with trypsin and the protease inhibitor TLCK (Fig. 7B and C). Similar studies were repeated with a physiologically-relevant concentration of enzyme. As shown in Figure 7D, a significant increase in fluorescence intensity was observed, although the rate and extent of fluorescence increase was lower in the time period recorded as expected. An increase in fluorescence intensity of more than threefold was achieved within 120 minutes, while about 5.5-fold and 7-fold increases were noted at 540 minutes and 24 hours, respectively.

Figure 7E shows a plot of the normalized fluorescence dynamics at 775 nm of EANPs exposed to trypsin, trypsin and TLCK, or buffer obtained in a 96-well microplate format. The results mimic those of Figure 7A–C, although a slight increase in fluorescence was observed with the sample exposed to both trypsin and TLCK. Regardless, the data demonstrate that a marked increase in fluorescence signal can be achieved upon enzymatic activation of the nanoprobes.

Since FITC-labeled nanoprobes (FITC-EANPs), instead of those labeled with AF750, were used in some of the experiments to allow microscopy in the visible range, similar studies were carried out with these nanoprobes to ensure that enzymatic activation would also be observed. Figure 8 shows the enzymatic development of fluorescence from FITC-labeled EANPs. FITC-labeled EANPs exhibited fluorescence quenching and protease-mediated activation similarly to AF750-labeled EANPs.

Cytocompatibility

The cytocompatibility of the EANPs was assessed with MDA-MB-231 cancer cells. Figure 9A shows the viability of cells exposed to AF750-labeled EANPs for 72 hours. Cells

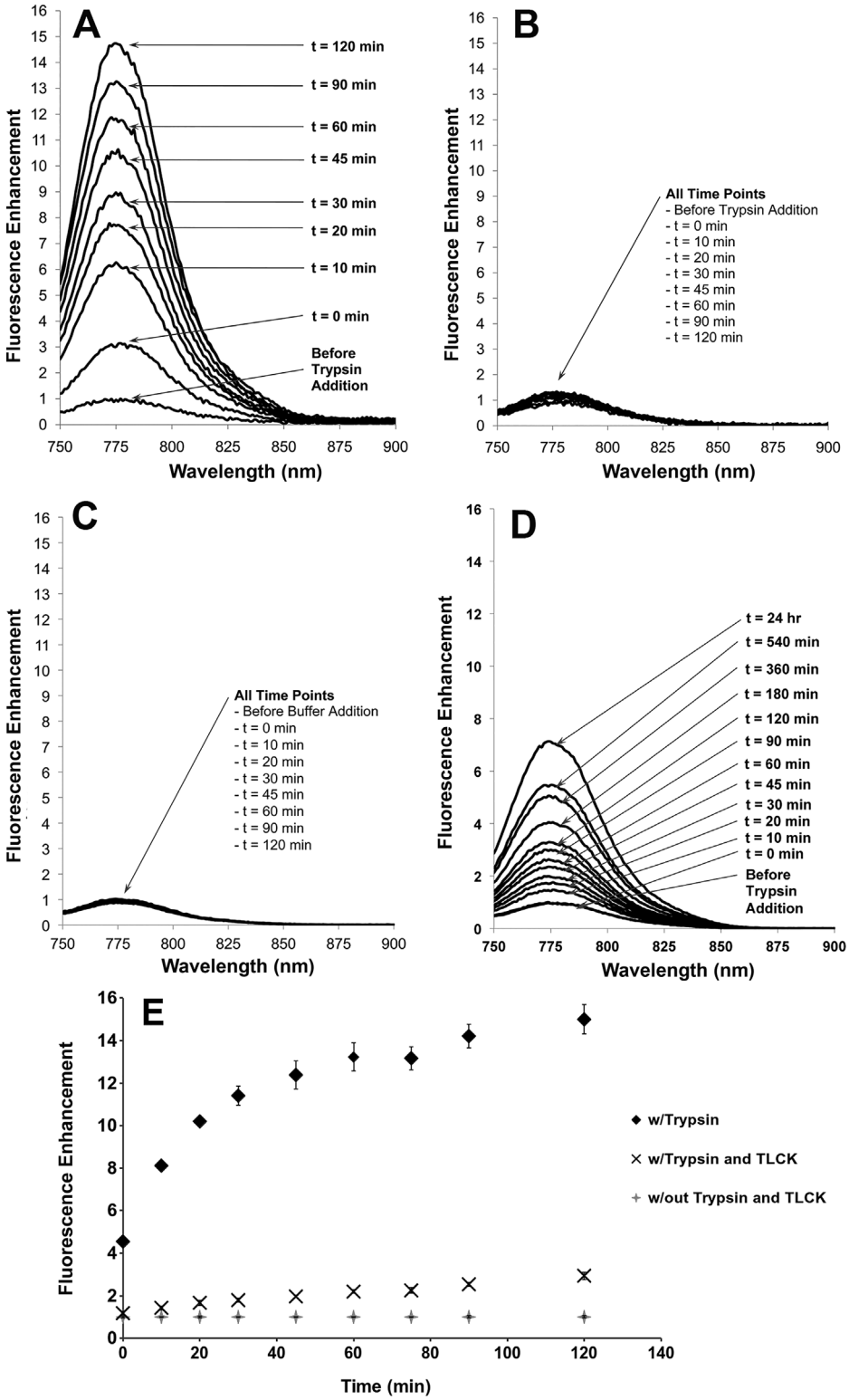

Fig. 7. In vitro enzymatic activation of EANP fluorescence. Fluorescence spectra of EANP suspensions at a concentration of 437.5 μg/ml exposed to **(A)** 2.5 mg/ml trypsin, **(B)** 2.5 mg/ml trypsin in the presence of 4 mg/ml protease inhibitor, **(C)** equivalent volume of PBS (control), and **(D)** 0.025 mg/ml trypsin. **E**: Plot of average fluorescence at 775 nm versus time for EANPs exposed to trypsin, trypsin and TLCK, or buffer. Error bars represent standard deviation ($n = 4$).

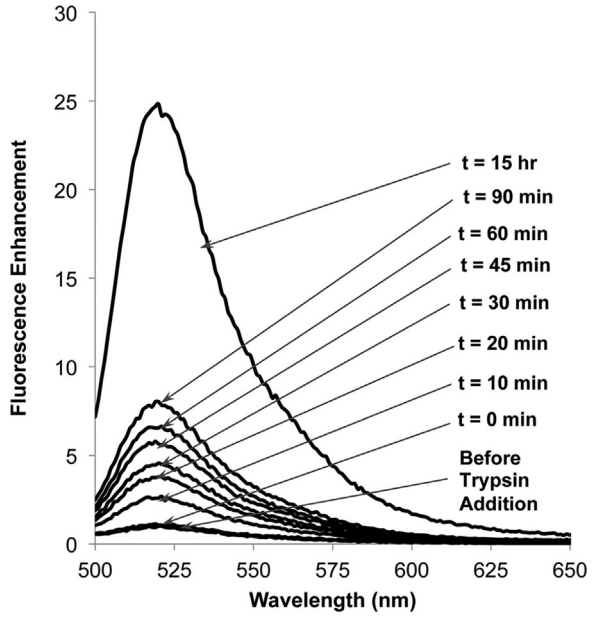

Fig. 8. Enzymatic activation of fluorescence of FITC-labeled EANPs. Similarly to AF750-labeled EANPs, FITC-labeled EANPs showed a significant increase in fluorescence upon treatment with the model enzyme trypsin.

exposed to EANPs showed high viability (87–100% of control), even at high concentrations. Neither a general dose-dependent viability trend nor a statistically significant difference was observed in these studies ($P > 0.15$ for all samples). As expected, the negative viability control alone had statistically lower viability ($P < 0.05$). In addition to quantitative viability determination via the MTT assay, cells were monitored via microscopy during the studies and no visual differences in cell morphology or growth were observed between EANP-treated NPs compared to cells in the positive viability control set. These studies overall suggest that the EANPs are biocompatible.

Interaction of Nanoprobes With Cultured Cells

Reflectance, fluorescence, and overlay images of nanoprobe-cell interaction are shown for samples of cancerous (MDA-MB-231) and noncancerous (HDF) cells that were exposed to FITC-labeled EANPs for 36 hours. These studies were carried out with FITC-labeled EANPs to allow for imaging in the visible range. Fluorescence was not observed from cells that were not exposed to EANPs (data not shown). A low level of fluorescence was observed on fibroblast cells exposed to EANPs (Fig. 9B). An increase in fluorescence was observed on the surface and within the cytoplasm of MDA-MB-231 cancer cells exposed to EANPs (Fig. 9C).

In comparison to fibroblasts, cancer cells are known to overexpress proteases. It is possible that a higher level of protease activity in the cancer cells is at least partly responsible for the increased fluorescence levels of EANP in these cells as compared to the noncancerous cells, although differing characteristics of the two cell lines could also be important factors. For example, the two cell lines might have differing rates of endocytosis, which could influence the extent of intracellular uptake of the nanoprobes, leading to differences in fluorescence intensities that are not completely caused by the enzymatic activation of the nanoprobes. The dependence of endocytic rates on fluorescent agent or nanoparticle identity, time of exposure, and cell line has been previously reported for benign and malignant cell lines of different metastatic potential [51–53]. For this reason, additional studies were conducted with MDA-MB-231 breast cancer cells to study the effect of enzymatic activity on fluorescence development. Figure 10 shows the transmission and NIR fluorescence images of the cells exposed to a constant concentration of EANPs but varying concentrations of the protease inhibitor TLCK. Increased TLCK concentrations prevented the activation of EANPs, leading to undetectable fluorescence in the cells compared to background. TLCK dose-dependency was observed in all samples with TLCK concentrations between 7.8 and 250 μM. These studies thus demonstrate the potential ability of the EANPs to interact with and be internalized into cells resulting in enzymatically-aided contrast enhancement.

In Vitro NIR Imaging in Tissue Phantoms

Enzymatically activated EANPs were imaged within tissue phantoms to investigate the effect of AF750-labeled EANP concentration and depth on imaging ability. Fluorescence emission decreased (i) as the depth within the tissue phantom increased, and (ii) as the concentration of activated EANPs within the suspension decreased (Fig. 11A). A contrast-to-background ratio greater than unity was observed even at the lowest EANP concentration of 28.4 μg/ml at up to a depth of 4 mm into the tissue phantom. As we did not study lower EANP concentrations, we anticipate that lower EANP concentrations may be detectable with the use of a laser/filter system that better matches the spectral properties of AF750. In this experiment, EANPs were excited with a 664 nm laser, which is blue shifted from the peak absorption of this fluorophore. Similarly, fluorescence emission was collected at wavelengths above 800 nm which are longer than the peak wavelength of AF750. Nonetheless, between 2.5 and over 13-fold increased fluorescence levels were detected with enzymatically activated EANPs (Fig. 11).

DISCUSSION

In this work, polymeric nanoprobes were developed as highly specific fluorescence-based contrast agents for cancer. Compared to other imaging technologies such as magnetic resonance imaging (MRI), computed tomography (CT), single photon emission computed tomography (SPECT), and positron emission tomography (PET), fluorescence-based imaging can offer high resolution, the ability to resolve spectral features of tissue or contrast agents, relative simplicity, and low cost, and avoids the use

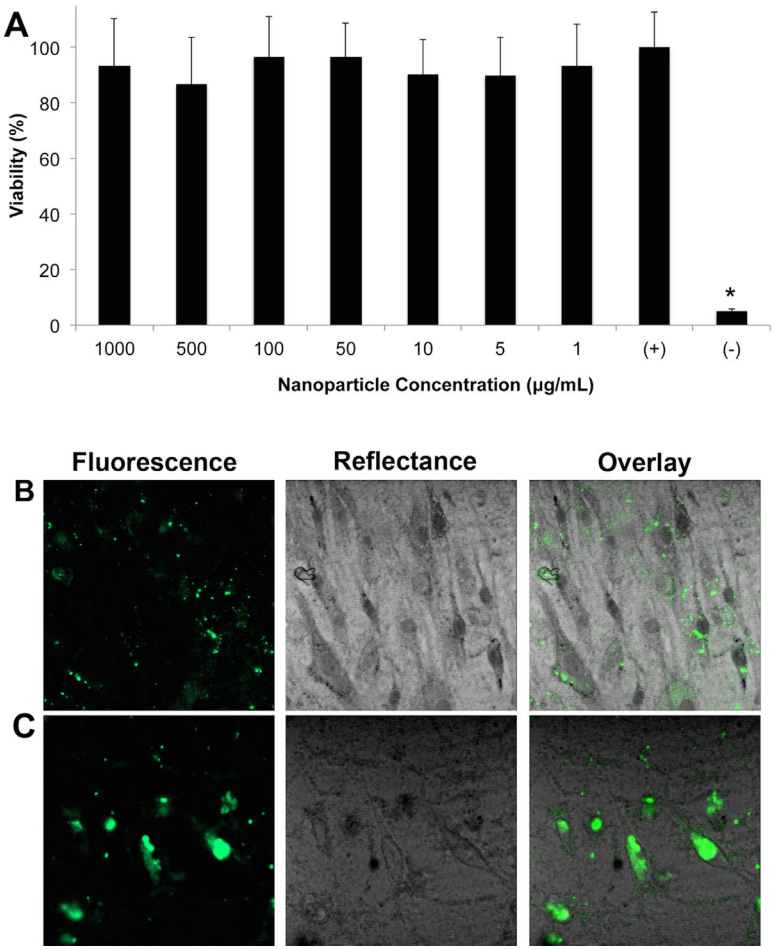

Fig. 9. Interaction of EANPs with cultured cells. **A**: Viability of MDA-MB-231 cells after exposure to EANP 72 hours determined with MTT assay. Cells cultured in complete media without EANPs represent the positive control (+). Cells killed with methanol prior to MTT assay represent negative control (−). Bars represent standard deviation. Statistically significant difference compared to positive control ($P < 0.05$) is identified with an asterisk (*). Representative fluorescence, reflectance and overlay images of cells exposed to EANP suspensions for 36 hours. **B**: HDF cells exposed to FITC-labeled EANPs. **C**: MDA-MB-231 cells exposed to FITC-labeled EANPs. Microscopy images were taken with a 40× objective.

of ionizing radiation. Fluorescent probes that provide disease specificity and increased signal-to-noise ratio through disease-mediated activation have been previously reported. Among these are multi-step bioorthogonal probes such as those that rely on the rapid and specific cycloaddition reaction between strained trans-cyclooctene or cyclooctyne-modified homing ligands and tetrazine or azide-functionalized fluorescent molecules [54–57]. These orthogonal probes, while effective at providing high signal-to-noise ratio, would require sequential delivery of the two components to the location of interest and are thus best suited for *in vitro* cell imaging.

Enzymatically-activated NIR fluorescent probes based on macromolecules that can interact with proteases overexpressed by tumors have also been developed [7–13], as discussed in the introduction. In addition to cancer applications, the use of protease-activated probes has been demonstrated in pancreatitis [14], a disease in which endoprotease activation is considered as one of the onset events; pulmonary inflammation [15]; atherosclerosis in which secreted proteolytic enzymes play a role in plaque disruption and associated complications [16–21]; and stent-induced inflammation [19]. Protease-activated probes based on PEGylated poly(L-lysine) have also been used as contrast agents for imaging infarcted myocardial tissue utilizing time-resolved fluorescence imaging [22]. A family of macromolecular enzymatically activated probes, including Prosense® and MMPSense®, is now commercially available (PerkinElmer, Inc.).

More recently, peptidic probes including both fluorescent molecules and quenchers have been used for *in vivo* imaging of tumor fibroblast activation protein a (FAPa) peptidase in mice [58] and matrix metalloproteinases in osteoarthritis and cancer [59,60]. Enzymatically activated

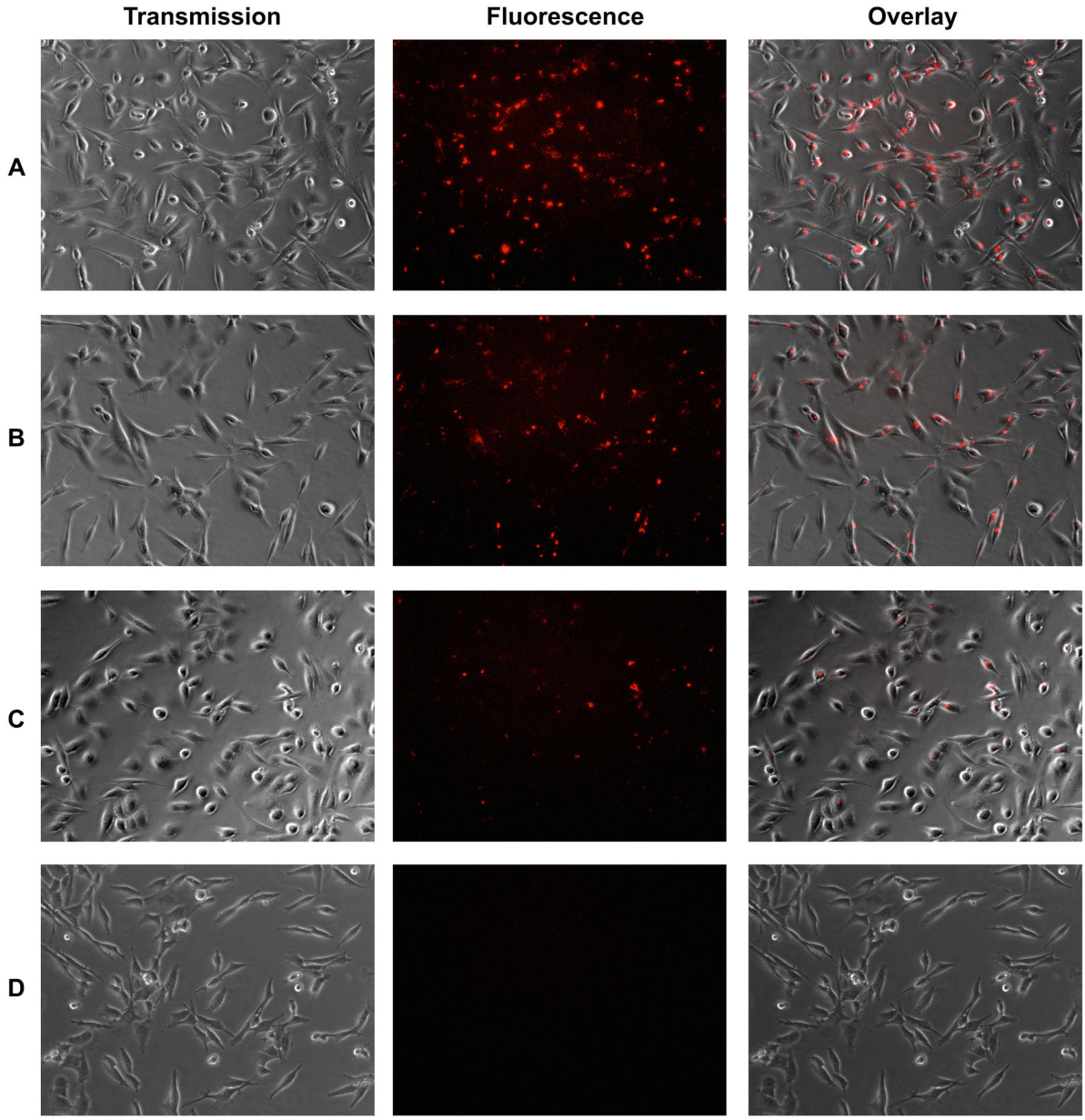

Fig. 10. Enzymatic Activation of Fluorescence in Cells. Transmission, NIR fluorescence, and overlay images of MDA-MB-231 cells exposed to AF750-labeled EANPs in the presence of varying concentrations of TLCK protease inhibitor: **(A)** 0.5 mg/ml EANPs and 0 μM TLCK, **(B)** 0.5 mg/ml EANPs and 31.25 μM TLCK, **(C)** 0.5 mg/ml EANPs and 250 μM TLCK, **(D)** 0 mg/ml EANPs and 0 μM TLCK.

cell penetrating peptides consisting of hairpin structures linked together by a cleavable linker have been also recently used as thrombin-activated fluorescent contrast agents for atherosclerotic plaque [61] and as intracellular drug delivery systems in protease-overexpressing tumors [62]. Peptide dendrimers or branched structures containing cathepsin S peptide substrates as linkers for NIR fluorochromes have also been reported [63]. Similarly, enzymatically cleavable polypeptides have been used for the development of enzymatically controlled drug delivery system in the past [64,65].

In addition to macromolecular contrast agents, research has begun on the development of nanoparticle-based activatable fluorescent nanoprobes. Crosslinked iron oxide nanoparticles have been used as carriers for NIR fluorescent dyes for combined magnetic resonance and optical imaging [23–25]. Gold [26], silica [27], and chitosan [28] nanoparticles have been more recently used as carriers for enzymatically activated fluorescent probes.

Compared to other nanoparticle-based protease probes [26–28], the EANPs herein described offer a number of benefits. Compared to gold and silica based

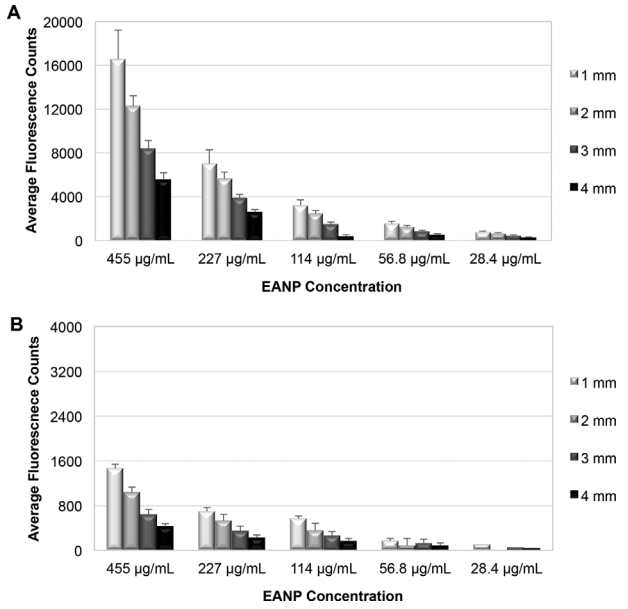

Fig. 11. NIR imaging in tissue phantoms. Depth-fluorescence intensity plot for decreasing EANP suspension concentrations. At each depth, bars show the average fluorescence counts at EANP concentrations from 28 to 455 µg/ml. Error bars represent the standard deviation of counts within region of interest in tissue phantom. **A**: EANPs activated with trypsin. **B**: EANPs diluted with buffer only.

systems [26,27], EANPs combine proven biocompatible and biodegradable polymers that easily assemble into core-shell nanostructures and that have been utilized as biomaterials in the drug delivery field for decades. Compared to polymeric protease activated nanoparticles [28], EANPs were also designed to include surface modifications to enhance blood circulation and for incorporation of targeting agents, cancer-specific cleavable linkers for enzymatic development of NIR fluorescence, high loading of NIR fluorescent molecules, and a stable yet degradable core that could act as a drug reservoir in future studies. This combination of properties is expected to offer significant improvements in selectivity and sensitivity that would encourage their use in clinical settings as contrast agents for non-invasive detection, monitoring of cancer, or fluorescence-guided tumor treatment. In addition to their applications in cancer imaging, EANPs could be utilized in the study of physiological enzyme kinetics, and in the detection and monitoring of enzyme-related diseases such as inflammation and vascular disease.

Nanoprecipitation of amphiphilic copolymer blends enabled facile assembly of multi-component nanoprobes. FTIR analysis corroborated incorporation of all copolymers within the nanoprobe structure. Polymer blends were utilized for facile inclusion of the two hydrophilic polymers PLL and PEG on the surface of the nanoprobes. Specifically, each of the two copolymers consisted of a single hydrophilic (PLL or PEG) and a single hydrophobic region (PLGA or PLA). The architecture of these copolymers enabled self-assembly of the nanoprobes into a core-shell structure in which the hydrophilic components were presented on the surface and interacted with the surrounding aqueous environment. The use of copolymer blends enables easy modification of the ratio of PLL and PEG presented on the surface of the nanoprobes simply by changing the mass ratios of the PLGA-PLL to PLA-PEG used for nanoprobe preparation, without the need for further synthesis of branched copolymers containing both PLL and PEG. The hydrophobic portions of the copolymers form the core of the nanoprobe. PLGA and PLA, both hydrophobic biodegradable polyesters, were utilized in this work to provide EANPs with drug loading capabilities that will be investigated in future work. These hydrophobic polymer blocks could be replaced with only PLGA (including PLGA polymers of different lactide-to-glycolide ratio), only PLA, or even other hydrophobic polymers as needed to tune the biodegradation and drug loading capacity of the nanoprobes.

The ability to fluorescently label the nanoprobes after nanoassembly confirmed surface localization of PLL chains, as well as relatively hydrophilic and flexible environment of the nanoprobe shell. Dynamic light scattering and electron microscopy confirmed the nanoscaled size and spherical morphology of EANPs (Fig. 6).

Unlike other contrast agents, EANPs are designed to provide both structural and functional information about the target tissue since their enzymatic dependence can convey clues about disease status and prognosis. Proteolytic enzymes play numerous roles in animal physiology and pathophysiology. Many diseases, including cancer, arteriosclerosis, inflammation, and vascular disease are associated with abnormal enzymatic activity [66]. Elevated expression of cathepsin B and D has been observed in ovarian, lung, colorectal, and breast cancer tissue, and has been correlated with poor patient prognosis [67–70]. Proteases have been investigated as triggers for drug delivery [65] and imaging of pathological events in combination with NIR fluorescent probes. Results of studies of *in vitro* enzymatic fluorescence activation with the model protease trypsin and in cultured cancer cells demonstrated the capabilities of our EANPs as enzymatically triggered contrast agents. PLL acted as an enzymatically cleavable carrier for NIR fluorescent molecules. Rationally functionalized polypeptide sequences that are known substrates to specific cathepsins and matrix metalloproteinases will be utilized instead of PLL in the future to provide more disease-specific activation. For example, polypeptide substrates containing the PLGVR amino acid sequence show selectivity for matrix metalloproteinases while the GFLG tetra peptide can be cleaved by cysteine proteases including Cathepsins B, H, L, and C [26,65,71,72].

Imaging studies in tissue phantoms showed the promising capabilities of EANPs as optical contrast agents for *in vivo* applications. As opposed to fluorescent molecules that absorb and emit light in the visible range, NIR imaging enables interrogation of deeper tissue due to minimal spectral overlap with physiological chromophores. In this work we have demonstrated our ability to detect

fluorescence from EANPs at concentrations as low as 28 μg/ml up to a depth of 4 mm within phantoms of optical properties similar to those of tissue (Fig. 11). Enzymatically activated EANPs showed significantly increased fluorescence compared to non-activated EANPs in these tissue phantom experiments, suggesting that these nanoprobes could potentially enable tumor-specific imaging and image-guided therapeutic interventions.

Future studies will investigate the potential of these contrast agents for *in vivo* imaging in animal models of cancer, as well as their evaluation as theranostic agents that could be used for concurrent tumor imaging and drug delivery. The key benefits provided by EANPs for *in vivo* imaging compared to other contrast agents will be their targeting potential and high signal-to-background ratio. Compared to other enzymatically activated optical contrast agents, the size of EANPs will enable passive tumor targeting due to the enhanced permeability and retention effect. In addition, EANPs can be actively directed to a target by conjugation of agents such as antibodies, aptamers, or peptides to terminal carboxylic acid groups of the PEG chains which rest on the surface of the nanoprobes. Finally, the low fluorescence level of the nanoprobes prior to enzymatic activation ensures optimal conditions for optical imaging due to low background fluorescence.

Nanotechnology offers the possibility of creating complex multi-functional structures that can provide solutions for numerous biomedical problems. EANPs are an example of such structures, offering a combination of properties that are key for a successful NIR optical contrast agent. Their macromolecular structure, in addition, can be envisioned as a depot for targeted drug delivery, thus enabling opportunities for the development of theranostic systems.

ACKNOWLEDGMENTS

Funding for this research was provided by the National Institutes of Health (NIH) Small Business Innovation Research (1R43 CA144129-01) to InnoSense LLC; the Texas Emerging Technology Fund (Start-up funds for TB) and the Welch Foundation (AI-0045) to Texas State University; and the Arnold and Mabel Beckman Foundation (www.beckman-foundation.com) and National Institutes of Health (R01 HD065536, P41 EB015890) to the University of California, Irvine. We are grateful to the following personnel from the University of California, Irvine: Professor Kenneth J. Longmuir for initial access to dynamic light scattering instrumentation and Professor Brian Wong for generously providing human dermal fibroblasts.

REFERENCES

1. American Cancer Society. Cancer Facts & Figures 2015. Atlanta, GA: American Cancer Society. 2015.
2. van Dam GM, Themelis G, Crane LM, Harlaar NJ, Pleijhuis RG, Kelder W, Sarantopoulos A, de Jong JS, Arts HJ, van der Zee AG, Bart J, Low PS, Ntziachristos V. Intraoperative tumor-specific fluorescence imaging in ovarian cancer by folate receptor-alpha targeting: first in-human results. Nat Med 2011;17:1315–1319.
3. Kishimoto H, Zhao M, Hayashi K, Urata Y, Tanaka N, Fujiwara T, Penman S, Hoffman RM. In vivo internal tumor illumination by telomerase-dependent adenoviral GFP for precise surgical navigation. Proc Natl Acad Sci USA 2009;106:14514–14517.
4. Sevick-Muraca EM. Translation of near-infrared fluorescence imaging technologies: emerging clinical applications. Annu Rev Med 2012;63:217–231.
5. Chatterjee DK, Fong LS, Zhang Y. Nanoparticles in photodynamic therapy: an emerging paradigm. Adv Drug Deliv Rev 2008;60:1627–1637.
6. Ntziachristos V, Bremer C, Weissleder R. Fluorescence imaging with near-infrared light: new technological advances that enable *in vivo* molecular imaging. Eur Radiol 2003;13:195–208.
7. Weissleder R, Tung CH, Mahmood U, Bogdanov A, Jr. In vivo imaging of tumors with protease-activated near-infrared fluorescent probes. Nat Biotechnol 1999;17:375–378.
8. Mahmood U, Tung CH, Bogdanov A, Jr, Weissleder R. Near-infrared optical imaging of protease activity for tumor detection. Radiology 1999;213:866–870.
9. Sheth RA, Upadhyay R, Stangenberg L, Sheth R, Weissleder R, Mahmood U. Improved detection of ovarian cancer metastases by intraoperative quantitative fluorescence protease imaging in a pre-clinical model. Gynecol Oncol 2009; 112:616–622.
10. Habibollahi P, Figueiredo JL, Heidari P, Dulak AM, Imamura Y, Bass AJ, Ogino S, Chan AT, Mahmood U. Optical imaging with a cathepsin B activated probe for the enhanced detection of esophageal adenocarcinoma by dual channel fluorescent upper GI endoscopy. Theranostics 2012;2:227–234.
11. Ding S, Eric Blue R, Chen Y, Scull B, Kay Lund P, Morgan D. Molecular imaging of gastric neoplasia with near-infrared fluorescent activatable probes. Mol Imaging 2012;11: 507–515.
12. Mito JK, Ferrer JM, Brigman BE, Lee CL, Dodd RD, Eward WC, Marshall LF, Cuneo KC, Carter JE, Ramasunder S, Kim Y, Lee WD, Griffith LG, Bawendi MG, Kirsch DG. Intraoperative detection and removal of microscopic residual sarcoma using wide-field imaging. Cancer 2012;118: 5320–5330.
13. Cuneo KC, Mito JK, Javid MP, Ferrer JM, Kim Y, Lee WD, Bawendi MG, Brigman BE, Kirsch DG. Imaging primary mouse sarcomas after radiation therapy using cathepsin-activatable fluorescent imaging agents. Int J Radiat Oncol Biol Phys 2013;86:136–142.
14. Agarwal A, Boettcher A, Kneuer R, Sari-Sarraf F, Donovan A, Woelcke J, Simic O, Brandl T, Krucker T. In vivo imaging with fluorescent smart probes to assess treatment strategies for acute pancreatitis. PLoS ONE 2013;8:e55959.
15. Haller J, Hyde D, Deliolanis N, de Kleine R, Niedre M, Ntziachristos V. Visualization of pulmonary inflammation using noninvasive fluorescence molecular imaging. J Appl Physiol 2008;104:795–802.
16. Chen J, Tung CH, Mahmood U, Ntziachristos V, Gyurko R, Fishman MC, Huang PL, Weissleder R. In vivo imaging of proteolytic activity in atherosclerosis. Circulation 2002;105: 2766–2771.
17. Deguchi JO, Aikawa M, Tung CH, Aikawa E, Kim DE, Ntziachristos V, Weissleder R, Libby P. Inflammation in atherosclerosis: visualizing matrix metalloproteinase action in macrophages *in vivo*. Circulation 2006;114:55–62.
18. Jaffer FA, Vinegoni C, John MC, Aikawa E, Gold HK, Finn AV, Ntziachristos V, Libby P, Weissleder R. Real-time catheter molecular sensing of inflammation in proteolytically active atherosclerosis. Circulation 2008;118:1802–1809.
19. Jaffer FA, Calfon MA, Rosenthal A, Mallas G, Razansky RN, Mauskapf A, Weissleder R, Libby P, Ntziachristos V. Two-dimensional intravascular near-infrared fluorescence molecular imaging of inflammation in atherosclerosis and stent-induced vascular injury. J Am Coll Cardiol 2011;57: 2516–2526.
20. Calfon MA, Rosenthal A, Mallas G, Mauskapf A, Nudelman RN, Ntziachristos V, Jaffer FA. In vivo near infrared

fluorescence (NIRF) intravascular molecular imaging of inflammatory plaque, a multimodal approach to imaging of atherosclerosis. J Vis Exp 2011;54:e2257.
21. Razansky D, Harlaar NJ, Hillebrands JL, Taruttis A, Herzog E, Zeebregts CJ, van Dam GM, Ntziachristos V. Multispectral optoacoustic tomography of matrix metalloproteinase activity in vulnerable human carotid plaques. Mol Imaging Biol 2012;14:277–285.
22. Goergen C, Chen H, Bogdanov A, Jr., Sosnovik D, Kumar A. In vivo fluorescence lifetime detection of an activatable probe in infarcted myocardium. J Biomed Opt 2012;17:056001.
23. Josephson L, Kircher MF, Mahmood U, Tang Y, Weissleder R. Near-infrared fluorescent nanoparticles as combined MR/optical imaging probes. Bioconjug Chem 2002;13:554–560.
24. Kircher MF, Weissleder R, Josephson L. A dual fluorochrome probe for imaging proteases. Bioconjug Chem 2004;15:242–248.
25. Salthouse CD, Reynolds F, Tam JM, Josephson L, Mahmood U. Quantitative measurement of protease-activity with correction of probe delivery and tissue absorption effects. Sens Actuators B Chem 2009;138:591–597.
26. Lee S, Cha EJ, Park K, Lee SY, Hong JK, Sun IC, Kim SY, Choi K, Kwon IC, Kim K, Ahn CH. A near-infrared-fluorescence-quenched gold-nanoparticle imaging probe for *in vivo* drug screening and protease activity determination. Angew Chem Int Ed Engl 2008;47:2804–2807.
27. Achatz DE, Mezo G, Kele P, Wolfbeis OS. Probing the activity of matrix metalloproteinase II with a sequentially click-labeled silica nanoparticle FRET probe. Chembiochem 2009;10:2316–2320.
28. Lee S, Ryu JH, Park K, Lee A, Lee SY, Youn IC, Ahn CH, Yoon SM, Myung SJ, Moon DH, Chen X, Choi K, Kwon IC, Kim K. Polymeric nanoparticle-based activatable near-infrared nanosensor for protease determination *in vivo*. Nano Lett 2009;9:4412–4416.
29. McDonald DM, Baluk P. Significance of blood vessel leakiness in cancer. Cancer Res 2002;62:5381–5385.
30. Yokoyama M, Okano T. Targetable drug carriers: present status and future perspectives. Adv Drug Deliv Rev 1996;21:77–80.
31. Folkman J. Fundamental concepts of the angiogenic process. Curr Mol Med 2003;3:643–651.
32. Folkman J, Merler E, Abernathy C, Williams G. Isolation of a tumor factor responsible for angiogenesis. J Exp Med 1971;133:275–288.
33. Whitney JR, Sarkar S, Zhang J, Do T, Young T, Manson MK, Campbell TA, Puretzky AA, Rouleau CM, More KL, Geohegan DB, Rylander CG, Dorn HC, Rylander MN. Single walled carbon nanohorns as photothermal cancer agents. Lasers Surg Med 2011;43:43–51.
34. Whitney J, DeWitt M, Whited BM, Carswell W, Simon A, Rylander CG, Rylander MN. 3D viability imaging of tumor phantoms treated with single-walled carbon nanohorns and photothermal therapy. Nanotechnology 2013;24:275102.
35. Pattani VP, Tunnell JW. Nanoparticle-mediated photothermal therapy: a comparative study of heating for different particle types. Lasers Surg Med 2012;44:675–684.
36. Lin AY, Almeida JP, Bear A, Liu N, Luo L, Foster AE, Drezek RA. Gold nanoparticle delivery of modified CpG stimulates macrophages and inhibits tumor growth for enhanced immunotherapy. PLoS ONE 2013;8:e63550.
37. Park J, Estrada A, Schwartz JA, Diagaradjane P, Krishnan S, Dunn AK, Tunnell JW. Intra-organ biodistribution of gold nanoparticles using intrinsic two-photon induced photoluminescence. Lasers Surg Med 2010;42:630–639.
38. Puvanakrishnan P, Diagaradjane P, Kazmi SM, Dunn AK, Krishnan S, Tunnell JW. Narrow band imaging of squamous cell carcinoma tumors using topically delivered anti-EGFR antibody conjugated gold nanorods. Lasers Surg Med 2012;44:310–317.
39. Prencipe G, Tabakman SM, Welsher K, Liu Z, Goodwin AP, Zhang L, Henry J, Dai H. PEG branched polymer for functionalization of nanomaterials with ultralong blood circulation. J Am Chem Soc 2009;131:4783–4787.
40. Torchilin VP. Which polymer can make nanoparticulate drug carriers long-circulating? Adv Drug Deliv Rev 1995;16: 141–155.
41. Avgoustakis K. Pegylated poly(lactide) and poly(lactide-co-glycolide) nanoparticles: preparation, properties and possible applications in drug delivery. Curr Drug Deliv 2004;1: 321–333.
42. Gref R, Luck M, Quellec P, Marchand M, Dellacherie E, Harnisch S, Blunk T, Muller RH. 'Stealth' corona-core nanoparticles surface modified by polyethylene glycol (PEG): influences of the corona (PEG chain length and surface density) and of the core composition on phagocytic uptake and plasma protein adsorption. Colloids Surf B Biointerfaces 2000;18:301–313.
43. Mehvar R. Modulation of the pharmacokinetics and pharmacodynamics of proteins by polyethylene glycol conjugation. J Pharm Pharm Sci 2000;3:125–136.
44. Otsuka H, Nagasaki Y, Kataoka K. PEGylated nanoparticles for biological and pharmaceutical applications. Adv Drug Deliv Rev 2003;55:403–419.
45. Betancourt T, Byrne JD, Sunaryo N, Crowder SW, Kadapakkam M, Patel S, Casciato S, Brannon-Peppas L. PEGylation strategies for active targeting of PLA/PLGA nanoparticles. J Biomed Mater Res A 2009;91:263–276.
46. Betancourt T, Brown B, Brannon-Peppas L. Doxorubicin-loaded PLGA nanoparticles by nanoprecipitation: preparation, characterization and *in vitro* evaluation. Nanomedicine (London) 2007;2:219–232.
47. Blum G, von Degenfeld G, Merchant MJ, Blau HM, Bogyo M. Noninvasive optical imaging of cysteine protease activity using fluorescently quenched activity-based probes. Nat Chem Biol 2007;3:668–677.
48. Da Costa V, Wei R, Lim R, Sun CH, Brown JJ, Wong BJ. Nondestructive imaging of live human keloid and facial tissue using multiphoton microscopy. Arch Facial Plast Surg 2008;10:38–43.
49. Saager RB, Kondru C, Au K, Sry K, Ayers F, Durking AJ. Multi-layer silicone phantoms for the evaluation of quantitative optical techniques in skin imaging. Proc SPIE 2010; 7567:756706.
50. Wang W, Tetley L, Uchegbu IF. A new class of amphiphilic poly--lysine based polymers forms nanoparticles on probe sonication in aqueous media. Langmuir 2000;16:7859–7866.
51. Gal M, Massalha S, Samuelly-Nafta O, Weihs D. Effects of particle uptake, encapsulation, and localization in cancer cells on intracellular applications. Med Eng Phys 2015;37:478–483.
52. Zhang Y, Ynag M, Portney NG, Cui D, Budak G, Ozbay E, Ozkan M, Ozkan CS. Zeta potential: a surface electrical characteristic to probe the interaction of nanoparticles with normal and cancer human breast epithelial cells. Biomed Microdevices 2008;10:321–328.
53. Li C, Greenwood TR, Glunde K. Glucosamine-bound near-infrared fluorescent probes with lysosomal specificity for breast tumor imaging. Neoplasia 2008;10:389–398.
54. Devaraj NK, Hilderbrand S, Upadhyay R, Mazitschek R, Weissleder R. Bioorthogonal turn-on probes for imaging small molecules inside living cells. Angew Chem Int Ed Engl 2010; 49:2869–2872.
55. Devaraj NK, Weissleder R. Biomedical applications of tetrazine cycloadditions. Acc Chem Res 2011;44:816–827.
56. Karver MR, Weissleder R, Hilderbrand SA. Bioorthogonal reaction pairs enable simultaneous, selective, multi-target imaging. Angew Chem Int Ed Engl 2012;51:920–922.
57. Devaraj NK, Thurber GM, Keliher EJ, Marinelli B, Weissleder R. Reactive polymer enables efficient *in vivo* bioorthogonal chemistry. Proc Natl Acad Sci USA 2012;109: 4762–4767.
58. Li J, Chen K, Liu H, Cheng K, Yang M, Zhang J, Cheng JD, Zhang Y, Cheng Z. Activatable near-infrared fluorescent probe for *in vivo* imaging of fibroblast activation protein-alpha. Bioconjug Chem 2012;23:1704–1711.
59. Ryu J, Lee A, Na J, Lee S, Ahn H, Park J, Ahn C, Kim B, Kwon I, Choi K, Youn I, Kim K. Optimization of matrix metalloproteinase fluorogenic probes for osteoarthritis imaging. Amino Acids 2011;41:1113–1122.
60. Yhee J, Kim S, Koo H, Son S, Ryu J, Youn I, Choi K, Kwon I, Kim K. Optical imaging of cancer-related proteases using near-infrared fluorescence matrix metalloproteinase-sensitive and cathepsin B-sensitive probes. Theranostics 2012;2:179–189.

61. Olson E, Whitney M, Friedman B, Aguilera T, Crisp J, Baik F, Jian T, Baird S, Tsimikas S, Tsien R, Nguyen Q. In vivo fluorescence imaging of atherosclerotic plaques with activatable cell-penetrating peptides targeting thrombin activity. Integr Biol (Camb) 2012;4:595–605.
62. Shi N, Gao W, Xiang B, Qi X-R. Enhancing cellular uptake of activable cell-penetrating peptide-doxorubicin conjugate by enzymatic cleavage. Int J Nanomedicine 2012;7:1613–1621.
63. Galande AK, Hilderbrand SA, Weissleder R, Tung CH. Enzyme-targeted fluorescent imaging probes on a multiple antigenic peptide core. J Med Chem 2006;49:4715–4720.
64. Singh HD, Bushnak I, Unsworth LD. Engineered peptides with enzymatically cleavable domains for controlling the release of model protein drug from "soft" nanoparticles. Acta Biomater 2012;8:636–645.
65. Glangchai LC, Caldorera-Moore M, Shi L, Roy K. Nanoimprint lithography based fabrication of shape-specific, enzymatically-triggered smart nanoparticles. J Control Release 2008;125:263–272.
66. Edwards DR, Murphy G. Cancer. Proteases-invasion and more. Nature 1998;394:527–528.
67. Liaudet-Coopman E, Beaujouin M, Derocq D, Garcia M, Glondu-Lassis M, Laurent-Matha V, Prebois C, Rochefort H, Vignon F. Cathepsin D newly discovered functions of a long-standing aspartic protease in cancer and apoptosis. Cancer Lett 2006;237:167–179.
68. Heidtmann HH, Salge U, Abrahamson M, Bencina M, Kastelic L, Kopitar-Jerala N, Turk V, Lah TT. Cathepsin B and cysteine proteinase inhibitors in human lung cancer cell lines. Clin Exp Metastasis 1997;15:368–381.
69. Werle B, Kraft C, Lah TT, Kos J, Schanzenbacher U, Kayser K, Ebert W, Spiess E. Cathepsin B in infiltrated lymph nodes is of prognostic significance for patients with nonsmall cell lung carcinoma. Cancer 2000;89:2282–2291.
70. Campo E, Munoz J, Miquel R, Palacin A, Cardesa A, Sloane BF, Emmert-Buck MR. Cathepsin B expression in colorectal carcinomas correlates with tumor progression and shortened patient survival. Am J Pathol 1994;145:301–309.
71. Bremer C, Tung CH, Weissleder R. In vivo molecular target assessment of matrix metalloproteinase inhibition. Nat Med 2001;7:743–748.
72. Minko T, Kopeckova P, Kopecek J. Efficacy of the chemotherapeutic action of HPMA copolymer-bound doxorubicin in a solid tumor model of ovarian carcinoma. Int J Cancer 2000;86:108–117.